Theory of plasmonic properties of hyper-doped silicon nanostructures

Clément Majorel, Vincent Paillard, Adelin Patoux, Peter Wiecha, Aurelien Cuche, Arnaud Arbouet, Caroline Bonafos, Christian Girard

Theory of plasmonic properties of hyper-doped silicon nanostructures

Clément Majorel[a,*], Vincent Paillard[a], Adelin Patoux[a], Peter R. Wiecha[a,1], Aurélien Cuche[a], Arnaud Arbouet[a], Caroline Bonafos[a], Christian Girard[a,*]

[a] *CEMES-CNRS, Université de Toulouse, CNRS, UPS, 29 rue Jeanne Marvig, 31055 Toulouse, France.*

Abstract

The presence of a Localized Surface Plasmon Resonance in doped semiconductor nanostructures opens a new field for plasmonics and metasurfaces. Semiconductor nanostructures can be easily processed, have weak dissipation losses, and the plasmon resonance can be tuned from the mid- to the near-infrared spectral range by changing the dopant concentration (in complement to the constituent material, the size and shape of the nanostructure). We present in this paper an extension of the Green Dyadic Method applied to the case of doped silicon nanostructures of arbitrary shape on a planar silica substrate. The method is used to compute both far- and near-fied optical properties, such as the extinction efficiency and the electromagnetic near-field intensity inside and around any doped silicon nanostructure, respectively. This theoretical approach provides an important tool for active dopant characterization in doped semiconductor nanostructures, for near-field imaging of complex nanoantennas produced by electron beam lithography, and for the definition of doped semiconductor-based metasurfaces.

Keywords: Surface plasmons, Hyperdoped nanostructures, Silicon

During the three last decades, a huge amount of work has been devoted to the understanding of the plasmonic properties of complex metallic nanostructures, either individually or as the elementary brick of a metamaterial. This interest was also driven by potential applications in sensing devices [1], nanophotonic devices [2], photocatalysis [3], and field-enhanced spectroscopies [4, 5, 6, 7]. However, the use of metals such as gold or silver is still an issue due to a poor compatibility with the semiconductor processing technology, and to strong dissipation losses at optical and infrared frequencies.

Recently, a new category of plasmonic materials emerged, with the study of Localized Surface Plasmon Resonance (LSPR) in heavily doped semiconductor nanostructures and metamaterials [8, 9, 10, 11]. Compared to metals, the imaginary part of the dielectric constant in the visible and infrared range is low for most semiconductors, leading to weak losses. As for metals, the LSPR frequency is tunable by the constituent material, the size and shape of the nanostructure, and its dielectric environment. However, the active dopant concentration, thus the free carrier (electrons or holes) concentration, allows to finely tune the LSPR frequency [8, 10]. Notably, the lower order of magnitude of carrier density in degenerate semiconductors with respect to noble metals has an attractive consequence: even a minor modification of the carrier density has a strong effect on the spectral position of the LSPR. Quantum size effects have also an influence in the case of nanocrystals of a few nanometers in diameter [12]. For larger nanostructures, for which the Drude model can be used, the LSPR frequency is varying from the far-infrared (FIR) range for standard dopant concentration (a few 10^{18} - 10^{19} cm^{-3}) to the mid-infrared range (MIR) for heavily doped semiconductors (about 10^{20} cm^{-3}), and even near-infrared (NIR) if higher concentration can be obtained (above 10^{21} cm^{-3}) [8]. Nonstoechiometric alloy nanocrystals, such as $Cu_{2-x}S$ or $Cu_{2-x}Se$, or metal-doped metal oxyde compounds (such as Al- or In-doped ZnO for instance) have shown intense plasmon resonances in the MIR to the NIR [8, 10, 11]. Few theoretical ab initio [12, 13, 14] and experimental [9, 12, 15, 16] work concern heavily doped silicon nanocrystals (Si-NCs), which are potentially interesting nanomaterials for plasmonic applications in the infrared due to their low cost and low toxicity. However, nanocrystals are difficult to handle and ordered arrays of nanostructures are needed for many applications, for instance infrared sensing as described in ref [5]. Therefore, doping Si nanostructures (Si-NS) as the ones produced by electron beam lithography in the thin Si overlayer of a Silicon On Insulator (SOI) substrate could be attractive candidates for such applications [17]. High dopant concentrations are actually achievable in Si by using out of equilibrium methods as nanosecond Laser Thermal Annealing (LTA) treatments. Hence, active phosphorus concentrations as high as 5×10^{20} cm^{-3} up to 2×10^{21} cm^{-3} can be reached in respectively thin SOI [19] and bulk silicon [18]. Recently doping Si with

*Corresponding author

Email address: clement.majorel@cemes.fr, girard@cemes.fr (Christian Girard)

[1] now with *Physics and Astronomy, Faculty of Engineering and Physical Sciences, University of Southampton, Southampton, UK.*

deep chalcogen donor as Te by using the same non equilibrium processing allows also exceeding 10^{21} cm^{-3} active dopants [20]. This doping range corresponds to a plasmon resonance wavelength of about 1.5 μm of great interest in photonics. It is thus important to develop theoretical tools able to describe the far-field and near-field electromagnetic properties of doped Si-based plasmonic nanoantennas of arbitrary size and shape, in a similar way as for the metal-based plasmonic nanoantennas. In the following, we will focus on Si-NS with dopant concentration in the 10^{20} to $5{\times}10^{21}$ cm^{-3} range and dimensions of a few tenths to a few hundreds of nanometers on top of a silica layer which mimics the SOI buried oxyde layer.

We introduce the Green Dyadic Method (GDM) implemented in the python toolkit pyGDM [21, 22]. GDM is an *ab–initio* electrodynamic method that relies on solving Maxwell's equations using Green's dyadic functions [22]. This method is interesting because calculations can be performed for nanostructures of arbitrary size, shape, composition and, in the context of doped semiconductor NS, of dopant concentration. We show that, by solving self–consistent equations, it is possible to determine both electric and magnetic fields at optical or infrared frequencies inside and outside a set of Si-based plasmonic nanostructures of arbitrary size and shape. Thus, all physical quantities such as extinction, absorption and scattering spectra, as well as near–field maps, can be calculated with precision [22].

1. The Green Dyadic Method (GDM) for submicrometer scale hyperdoped silicon structures

In the presence of an external illumination by an incident electromagnetic field characterized by the couple of electric and magnetic fields, $\{\mathbf{E}_0(\mathbf{r},t);\mathbf{H}_0(\mathbf{r},t)\}$, the local electric field $\mathbf{E}(\mathbf{r},t)$ induced inside and around a doped semiconductor system composed of N similar or different particles (see the illustrating example in figure (1)) can be calculated using the dyadic Lippmann–Schwinger equation:

$$\mathbf{E}(\mathbf{r},\omega) = \mathbf{E}_0(\mathbf{r},\omega) + \frac{1}{4\pi}\sum_{j=1}^{N}\int_{V_j}(\epsilon^j_{dop}(\omega)-\epsilon_{env}(\omega))\mathbf{S}(\mathbf{r},\mathbf{r}',\omega)\cdot\mathbf{E}(\mathbf{r}',\omega)d\mathbf{r}' \quad (1)$$

where $\mathbf{E}_0(\mathbf{r},\omega)$ and $\mathbf{E}(\mathbf{r},\omega)$ are the *time Fourier transforms* of the incident and local electric fields (written in CGS Gaussian units), respectively. In this self-consistent equation, $\epsilon^{(j)}_{dop}(\omega)$ and $\epsilon_{env}(\omega)$ represent the permittivity of the j^{th} doped semiconductor nanostructure and the surrounding medium, respectively. Considering the sub–micrometer size of the nanostructures investigated here, we can apply the simple Drude model, which accurately describes the carrier dynamics in bulk doped semiconductors:

$$\epsilon^{(j)}_{dop}(\omega) = \epsilon_{intr}(\omega) - \frac{(\omega^j_p)^2}{\omega(\omega+i\gamma^j)} \quad (2)$$

where $\epsilon_{intr}(\omega)$ represents the dielectric constant of the intrinsic semiconductor and γ^j is the damping term due to the collisions. ω^j_p defines the plasma frequency associated with the free carrier concentration of the j^{th} particle:

$$\omega^j_p = \sqrt{\frac{4\pi N^j_{dop}e^2}{m^\star_o}} \quad (3)$$

where N^j_{dop}, e, and $m^\star_o$ define the carrier density (in cm^{-3}), the elementary charge, and the effective mass respectively. The effective mass was chosen equal to 0.3 times the mass of the electron [23]. For all the calculations in this article, we have arbitrarily chosen $\gamma^j = 0.1\omega^j_p$. This choice makes it possible to take into account the accumulation of defects in the structure when the doping concentration increases. To confirm the consistency of this choice, we calculated the free electron damping γ by using $\gamma = e/m^*_0\mu$ where μ represents the mobility of the electrons [24, 25]. In Ref. [23], the mobility lies between ∼360 and 425 cm^{2}V^{-1}s^{-1} when the concentration of P increases from 4% to 18%. These percentages correspond respectively to carrier densities equal to 2×10^{21}cm^{-3} and 9×10^{21}cm^{-3}. By using the above values for mobility and effective mass, we found $\gamma \simeq 1.63\times10^{13}$Hz and $\gamma \simeq 1.38\times10^{13}$Hz, respectively. In our calculations, N_{dop} lies between $1{\times}10^{20}$cm^{-3} and $5{\times}10^{21}$cm^{-3}, that means the number of impurities is less important than in the reference. If we replace N_{dop} in Eq. (3) by these two values and multiply ω^j_p by 0.1 we obtain $\gamma^j = 1.64\times10^{13}$Hz and $\gamma^j = 11.60\times10^{13}$Hz, respectively. Therefore by choosing $\gamma^j = 0.1\omega^j_p$, γ^j is higher than γ, hence we overestimate the number of collisions of the electrons inside the structure.

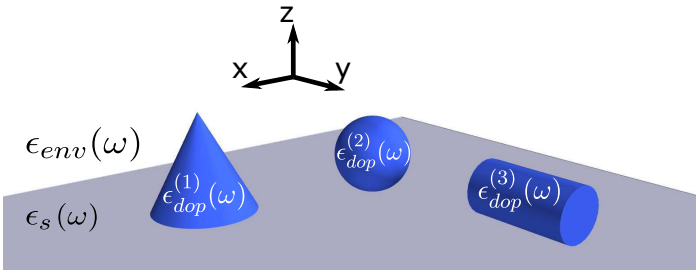

Figure 1: Example of three doped silicon nanostructures ($j = 1, 2,$ or 3) of both arbitrary shape and intrinsic doping parameters N^j_{dop}. These objects are lying on a plane silica substrate of optical index $n_s(\omega) = \sqrt{\epsilon_s(\omega)}$.

In Equation (1), the response function $\mathbf{S}(\mathbf{r},\mathbf{r}',\omega)$ is the Green dyadic tensor associated with the bare silica surface (*i.e.* computed in the absence of any nanostructure).

This second rank tensor matching the boundary conditions on the planar surface is given as the sum of two distinct contributions:

$$\mathbf{S}(\mathbf{r},\mathbf{r}',\omega) = \mathbf{S_0}(\mathbf{r},\mathbf{r}',\omega) + \mathbf{S}_{surf}(\mathbf{r},\mathbf{r}',\omega)\ , \tag{4}$$

where $\mathbf{S_0}(\mathbf{r},\mathbf{r}',\omega)$ represents the dipolar propagator of the homogeneous medium (characterized by $\epsilon_{env}(\omega)$), and $\mathbf{S}_{surf}(\mathbf{r},\mathbf{r}',\omega)$ takes into account the presence of the dielectric surface supporting the nanostructures:

$$\mathbf{S}_0(\mathbf{r},\mathbf{r}',\omega) = [k_0^2\mathbf{I} + \frac{1}{\epsilon_{env}(\omega)}\nabla_{\mathbf{r}}\nabla_{\mathbf{r}}]\frac{e^{ik|\mathbf{r}-\mathbf{r}'|}}{|\mathbf{r}-\mathbf{r}'|}, \tag{5}$$

with $k_0 = \omega/c$, $k = \sqrt{\epsilon_{env}(\omega)}\omega/c$, and

$$\mathbf{S}_{surf}(\mathbf{r},\,\mathbf{r}',\,\omega) = \frac{\Delta_{surf}(\omega)}{(X^2+Y^2+Z^2)^{5/2}}\times \begin{pmatrix} Z^2+Y^2-2X^2 & -3XY & 3XZ \\ -3XY & Z^2+X^2-2Y^2 & 3YZ \\ -3XZ & -3YZ & 2Z^2-Y^2-X^2 \end{pmatrix} \tag{6}$$

with $\mathbf{r} = (x,y,z)$, $\mathbf{r}' = (x',y',z')$, and $X = x'-x$, $Y = y'-y$, and $Z = z'+z$. The reflection coefficient $\Delta_{surf}(\omega)$ is given by:

$$\Delta_{surf}(\omega) = \frac{\epsilon_s(\omega)-\epsilon_{env}(\omega)}{\epsilon_s(\omega)+\epsilon_{env}(\omega)}\,. \tag{7}$$

As explained in reference [26], numerical solutions of (1) need a volume discretization of the source region occupied by the nanostructures. Generally, each particle volume V_j is discretized with n_j identical elementary volumes v_j. Such a procedure converts integrals into discrete summations:

$$\mathbf{E}(\mathbf{r},\omega) = \mathbf{E}_0(\mathbf{r},\omega) + \sum_{j=1}^{N}\eta_j(\omega)\sum_{i=1}^{n_j} \times [\mathbf{S}_0(\mathbf{r},\mathbf{r}_{j,i},\omega) + \mathbf{S}_{surf}(\mathbf{r},\mathbf{r}_{j,i},\omega)]\cdot\mathbf{E}(\mathbf{r}_{j,i},\omega)\ . \tag{8}$$

In this summation, the scalar parameters $\eta_j(\omega)$ are proportional to the elementary volumes v_j of the discretized cells in the j^{th} particle:

$$\eta_j(\omega) = \frac{\epsilon^{(j)}_{dop}(\omega)-\epsilon_{env}(\omega)}{4\pi}v_j\ , \tag{9}$$

and the vectors $\mathbf{r}_{j,i}$ define the positions of the discretized cells inside the j^{th} doped particle. The N nanostructures are positioned at the nodes of a cubic compact array. Notice that, in the case of most semiconductors including Si, the very high dielectric constant requires a fine discretization of the NS in order to have reliable calculations For instance a nanostructure with a dielectric constant $\mathrm{Re}\left\{\epsilon^{(j)}_{dop}\right\}$ illuminated by a plane wave of wavelength λ_0 leads to an effective wavelength in the material $\lambda_{eff} = \lambda_0/\sqrt{\mathrm{Re}\left\{\epsilon^{(j)}_{dop}\right\}}$. For a very high dielectric constant this effective wavelength may become comparable to the discretization step of the NS. In such case, the computation does not converge properly. The step d should be small compared to the wavelength inside the material and also with respect to the skin depth in an absorptive material [27].

2. Spectral and near–field optical properties of square shaped-doped silicon pads deposited on a silica surface

In the different sections of the paper, we will consider a normal incidence monochromatic plane wave as illumination mode. In this case, the incident electric field can be defined by:

$$\mathbf{E}_0(\mathbf{r},t) = \mathbf{E}_0\{\cos(\mathbf{k}\cdot\mathbf{r}-\omega_0 t) + \mathcal{F}_{env,surf}\cos(\mathbf{k}\cdot\mathbf{r}+\omega_0 t)\}\ , \tag{10}$$

where $\mathbf{k} = (0,0,-k)$ and $\mathbf{E}_0 = E_0(\cos(\phi),\sin(\phi),0)$ (in which ϕ labels the incident polarization angle), and $\mathcal{F}_{env,surf}$ defines the reflection Fresnel coefficient:

$$\mathcal{F}_{env,surf} = \frac{\sqrt{\epsilon_{env}(\omega)}-\sqrt{\epsilon_s(\omega)}}{\sqrt{\epsilon_{env}(\omega)}+\sqrt{\epsilon_s(\omega)}} \tag{11}$$

The Fourier transform of this field can be defined by:

$$\begin{aligned}\mathbf{E}_0(\mathbf{r},\omega) &= \frac{1}{2\pi}\int \mathbf{E}_0(\mathbf{r},t)e^{i\omega t}dt \\ &= \frac{\mathbf{E}_0}{2}(\{e^{i\mathbf{k}\cdot\mathbf{r}} + \mathcal{F}_{env,surf}e^{-i\mathbf{k}\cdot\mathbf{r}}\}\delta(\omega-\omega_0) \\ &+ \{e^{-i\mathbf{k}\cdot\mathbf{r}} + \mathcal{F}_{env,surf}e^{i\mathbf{k}\cdot\mathbf{r}}\}\delta(\omega+\omega_0))\end{aligned} \tag{12}$$

For hyperdoped silicon structures the external excitation wavelength $\lambda_0 = 2\pi c/\omega_0$ becomes an extremely sensitive parameter because of the known existence of plasmon resonances [8] and specific physical quantities can be used to characterize their new optical properties (near field intensity, absorption and scattering spectra, infrared local density of states, ...).

2.1. Case of a single cuboid nanostructure of doped Si (100×100×50 nm^3, N=1, n_1=4000)

(i) Extinction efficiency of a single doped Si pad

The extinction cross-section can be deduced from the local electric polarization induced inside the doped nanostructure (see figure (2d)):

$$C_{ext}(\lambda_0) = \frac{8\sqrt{\epsilon_{env}}\pi^2}{\lambda_0|E_0|^2}\sum_{j=1}^{N}\sum_{i=1}^{n_j}\Im(\mathbf{E}_0^{\star}(\mathbf{r}_{j,i},\lambda_0)\cdot\mathcal{P}(\mathbf{r}_{j,i},\lambda_0))\ , \tag{13}$$

where $\Im$ depicts the imaginary part and

$$\mathcal{P}(\mathbf{r}_{j,i},\omega_0) = \eta_j(\omega)\mathbf{E}(\mathbf{r}_{j,i},\omega_0) \tag{14}$$

A first example is shown in figure (2) for a square shaped pad of heavily doped (N_{dop} =8×10^{20} cm^{-3}) silicon standing on a silica substrate. The spectrum of the extinction efficiency Q_{ext} (the extinction cross-section divided by the geometrical cross-section) exhibits a well–defined plasmon peak located around 2.8 μm. The first resonance at 2.8 μm corresponds to the free carrier-induced LSPR. Interestingly, one can observe at longer wavelength a second spectral structure composed of different resonances, one of which dominating around 9.5 μm. This resonance, far from the plasmon band, is the signature of an optical phonon excitation inside the silica wafer supporting the doped Si-NS. Indeed, in the vicinity of 9.5 μm, the real part of the dielectric constant $\epsilon_s(\omega)$ of silica becomes rapidly negative while its imaginary part significantly increases [29, 30]. Consequently, the coefficient $\Delta_{surf}(\omega)$ in the surface propagator $\mathbf{S}_{surf}(\mathbf{r},\mathbf{r}',\omega)$ (see also Eq. (7)) resonates at the optical phonon frequency, yielding the additional peak at 9.5 μm in the extinction spectrum. In that case, silica phonons are excited by the virtual dipole image induced under the silica surface by the real dipole induced inside the Si-NS by the incident illumination field.

The behavior of the two absorption bands is evidenced in figure (3) giving the extinction efficiency for the same Si pad as function of the dopant concentrations in the 1×10^{20} - 3×10^{21} cm^{-3} range and the excitation wavelength. It can be seen that the LSPR band at short wavelength follows the square root of the carrier density, while the phonon band around 9.5 μm is rather insensitive to the Si-NS dopant concentration. At lower dopant concentration, a coupling between both resonances due to LSPR in Si-NS and phonon absorption in silica occurs. This kind of plasphonics phenomenon has been already studied in ref [31, 32, 33].

For a high dopant concentration, the LSPR band is localized in the 1.5 - 2 μm range. Such frequencies are accessible with strongly anisotropic gold structures. For instance, in ref [34], where nanorods of length 110 nm and radius 5 nm present a resonance at λ = 1170 nm. The use of hyperdoped Si-NS makes it possible to obtain the LSPR frequencies in the same NIR range even with isotropic structures.

(ii) Near–field intensity distribution around a single Si pad

The function $I_{nf}(\mathbf{R},\lambda_0)$ gives the variation of the normalized optical near–field intensity recorded at a given location $\mathbf{R}$ above the sample and for the incident wavelength λ_0. This signal can be computed for each location $\mathbf{R}$ from the total electric field and the incident electric field given by equations (8) and (12), respectively:

$$I_{nf}(\mathbf{R},\lambda_0) = |\mathbf{E}(\mathbf{R},\lambda_0)|^2/|\mathbf{E}_o(\mathbf{R},\lambda_0)|^2 \tag{15}$$

In order to get more insight on the impact of the dopant concentration, we calculated the infrared near–field intensity distributions of the electric field around the Si-NS for different wavelengths, and compared them to the case of intrinsic Si. In figure (4a), we show the scattering efficiency of a Si-NS with a dopant concentration N_{dop}=2.66×10^{21} cm^{-3} corresponding to a LSPR wavelength of about 1.54 μm (see solid dark curve in frame (a)). This wavelength corresponds to the state-of-the art active dopant concentration that can be obtained experimentally by pulsed laser annealing [18], and is of outmost interest in photonics. It indeed belongs to the optical telecommunication window and matches the emission of Erbium ions, which have been recently found new applications in Telecom-Band Quantum Optics [35].

Then we compute the normalized electric near field at two different locations shown in the inset of (4a), corresponding to a site at $\mathbf{R}$ = $(0,0,70)$ on top of the Si-NS (magenta cross), and to a lateral site at $\mathbf{R}$ = $(-60,0,70)$ (green cross). The near-field intensity distributions are shown in the two frames of figure (4b). The more striking feature is the presence of a strong contrast observed above the lateral site when changing the wavelength from 1200 μm to 1900 μm (see left frame of figure (4b)). The contrast change is less marked above the top site (right frame of figure (4b). For these wavelengths, the 2D maps of the electric field intensity distribution are given in (4c) and (4d). This reveals either the absence of contrast or a strong contrast around the doped Si-NS by controlling the excitation of the localized plasmons. By comparison, the maps computed around intrinsic Si-NS (4e) and (4f) are very similar independently of the wavelength. The absence of a strong local contrast in the case of the doped silicon can be explained by a vanishing contrast of the real parts of the permittivities between environment (ϵ_{env} = 1) and the doped silicon around λ_0 = 1.2 μm (close to the sign change of Re$\{\epsilon_{dop}\}$).

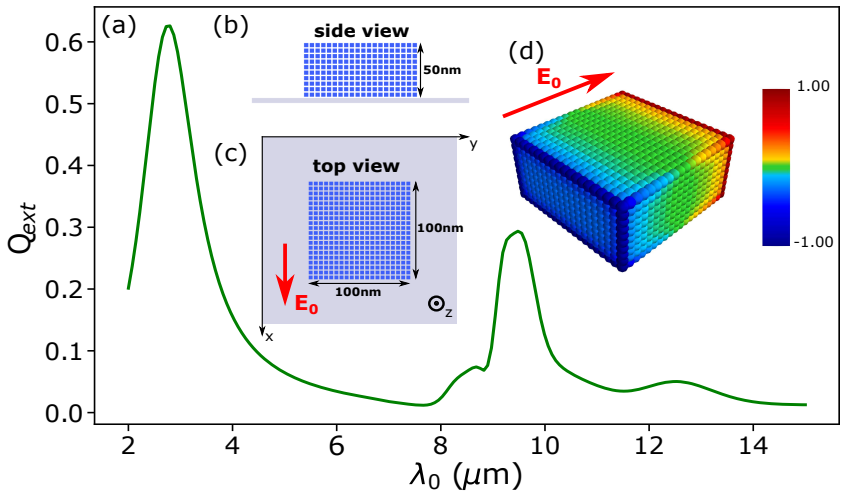

Figure 2: (a) Extinction efficiency spectrum computed for a single hyper-doped silicon cuboid structure of size $100 \times 100 \times 50$ nm^3 supported by a planar silica substrate. The dopant concentration N_{dop} is 8×10^{20} cm^{-3}. (b) Side view, and (c) top view of the discretized structure. Each point represents an elementary cell of volume v_i. $\mathbf{E}_0$ gives the incident plane wave polarization along the x-axis. (d) 3D representation of the snapshot of the charge density distribution inside the structure[28].

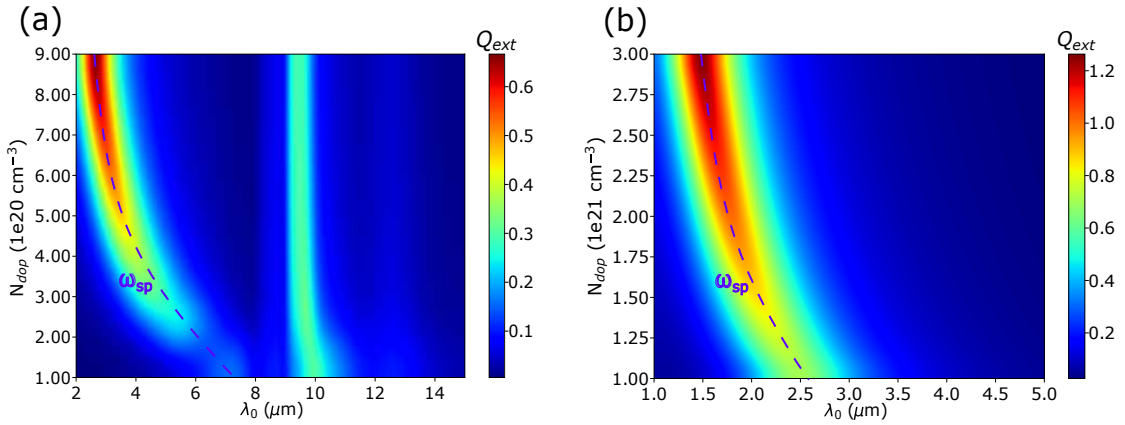

Figure 3: 2D map representation of the extinction efficiency for heavily doped cuboid Si-NS of size $100 \times 100 \times 50$ nm^3 lying on a silica substrate. The dopant concentration N_{dop} varies between 1×10^{20} and 9×10^{20} cm^{-3} (a) and 1×10^{21} and 3×10^{21} cm^{-3} (b). The purple dashed line represents the evolution of the LSPR as a function of the dopant concentration.

2.2. Case of randomly oriented and/or doped Si-NS:

In figure (5), we complete our simulation sequence with a set of $N = 5$ randomly located and oriented Si-NS excited by an incident plane wave. We remark first that the disordered arrangement of the particles tends to slightly downgrade the image–object relation observed with single particles (cf. figure (4)). In addition, we analyse the changes of the near–field intensity maps when gradually increasing the pad doping rate.

The analysis of these results raises the following comments.

(i) Although the system is illuminated in the s–polarized mode (incident electric field parallel to the substrate), each Si-NS (either intrinsic or doped) displays a typical contrast in the electric near–field intensity maps with a large field gradient near the Si-NS edges.

(ii) In the case of intrinsic Si, the contrast pattern does not depend on the incident wavelength. This is consistent with previous results reported in [36, 37], since in the absence of any plasmon resonance, those intrinsic Si-NS behave like dielectric pads.

(iii) Contrary, within a wavelength interval ranging from 1200 nm to 1850 nm centered around the plasmon resonance at $\lambda_r = 1540$ nm, we observe a significant change of the near–field intensity patterns when increasing the dopant concentration. In particular, close to $\lambda_0 = 1200$ nm, increasing the dopant concentration tends to flatten the contrast amplitude, illustrating how the incident wavelength can be used to control the visibility level expected in the *near–field zone* when approaching the plasmon resonance of the doped Si-NS.

3. Spectral and Polarization effect of a doped Si nanowire

Unlike doped cuboid Si-NS previously described, the ex-

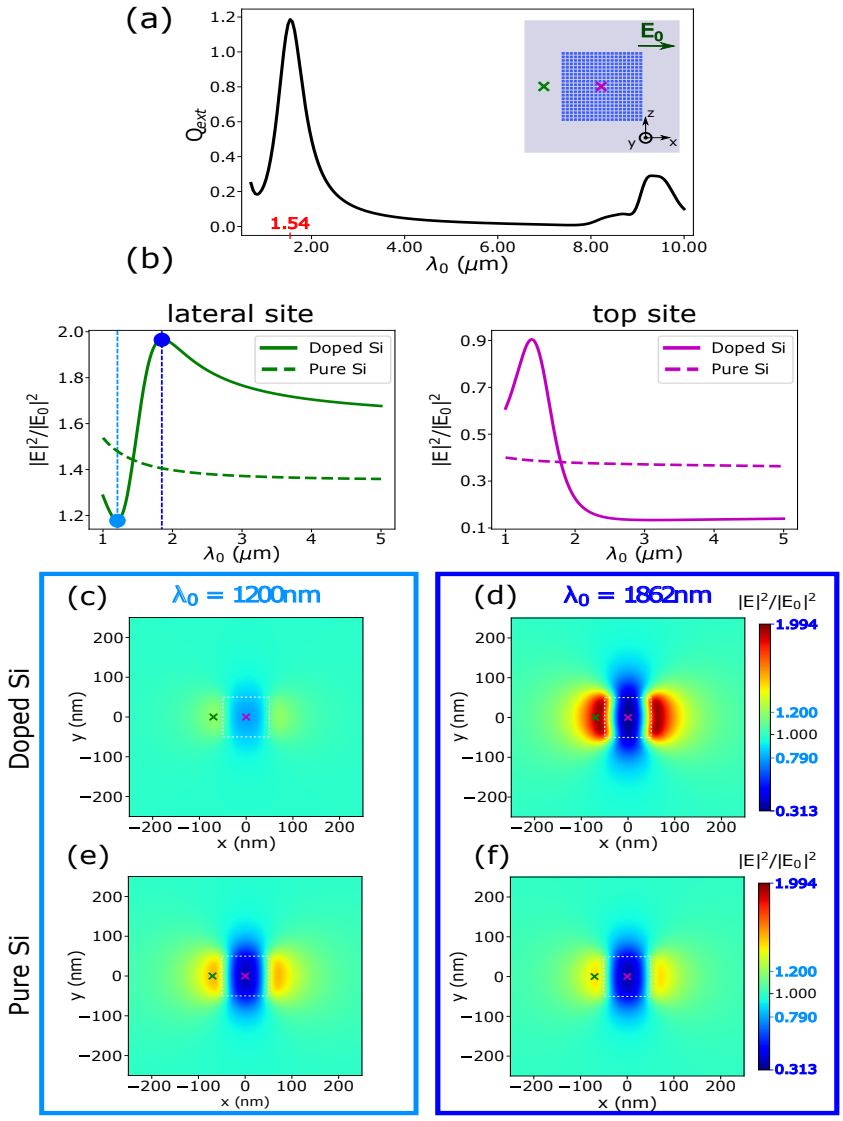

Figure 4: Simulation of the electric near–field behavior in the vicinity of doped ($N_{dop} = 2.66 \times 10^{21}$ cm^{-3}) and intrinsic single Si-NS of same geometrical cross–section ($100 \times 100 \times 50$ nm^3). (a) Top view geometry and extinction efficiency; (b) Local near–field optical spectra computed above two different sites defined by $\mathbf{R} = (-60, 0, 70)$ (lateral site) and $\mathbf{R} = (0, 0, 70)$ (top site). The blue dots indicate both minimum and maximum values of the near–field intensity above the edge of the doped Si-NS, occurring at $\lambda_0 = 1200$ nm and $\lambda_0 = 1862$ nm, respectively. (c)-(d) Corresponding near–field intensity maps computed in a plane $Z = 70$ nm;(e)-(f) Same maps as in (c)-(d) for intrinsic Si-NS.

tinction cross-section of anisotropic doped Si-NS such as nanowires exhibit two polarization-dependent plasmon bands, that correspond to carrier oscillations either along their length (longitudinal mode) or across their width (transverse mode). This behavior, presented in figure (6), is well-known in the field of the "standard" (metal) plasmonics, where it was realized that one of the most effective approach in plasmon engineering was to break the confinement symmetry by modifying the nanoparticle aspect ratio from spherical to rod shape [38, 39]. The symmetry breaking lifts the plasmon mode degeneracy and gives rise to two distinct transverse and longitudinal bands. In our case, the most striking result is that two distinct regions of the infrared spectrum can be investigated using doped semiconductor nanowires.

4. Conclusion and Perspectives

In Summary, we have adapted GDM to describe the enhanced light-matter interaction and electromagnetic field confinement in the case of sub-wavelength doped Si-based plasmonic nanostructures. We show that such properties can be tuned over the MIR and NIR spectral ranges as function of NS size, dopant concentration. In addition, modifying the aspect ratio leads to two distinct transverse and longitudinal modes by lifting the plasmon mode degeneracy. Our results provide a useful tool for active dopant concentration measurement in doped semiconductor nanostructures using infrared absorption experiments, and for modeling near–field imaging in the infrared.

As shape and/or dopant concentration allow obtaining LSPR near the telecom wavelength of 1.54 μm, there

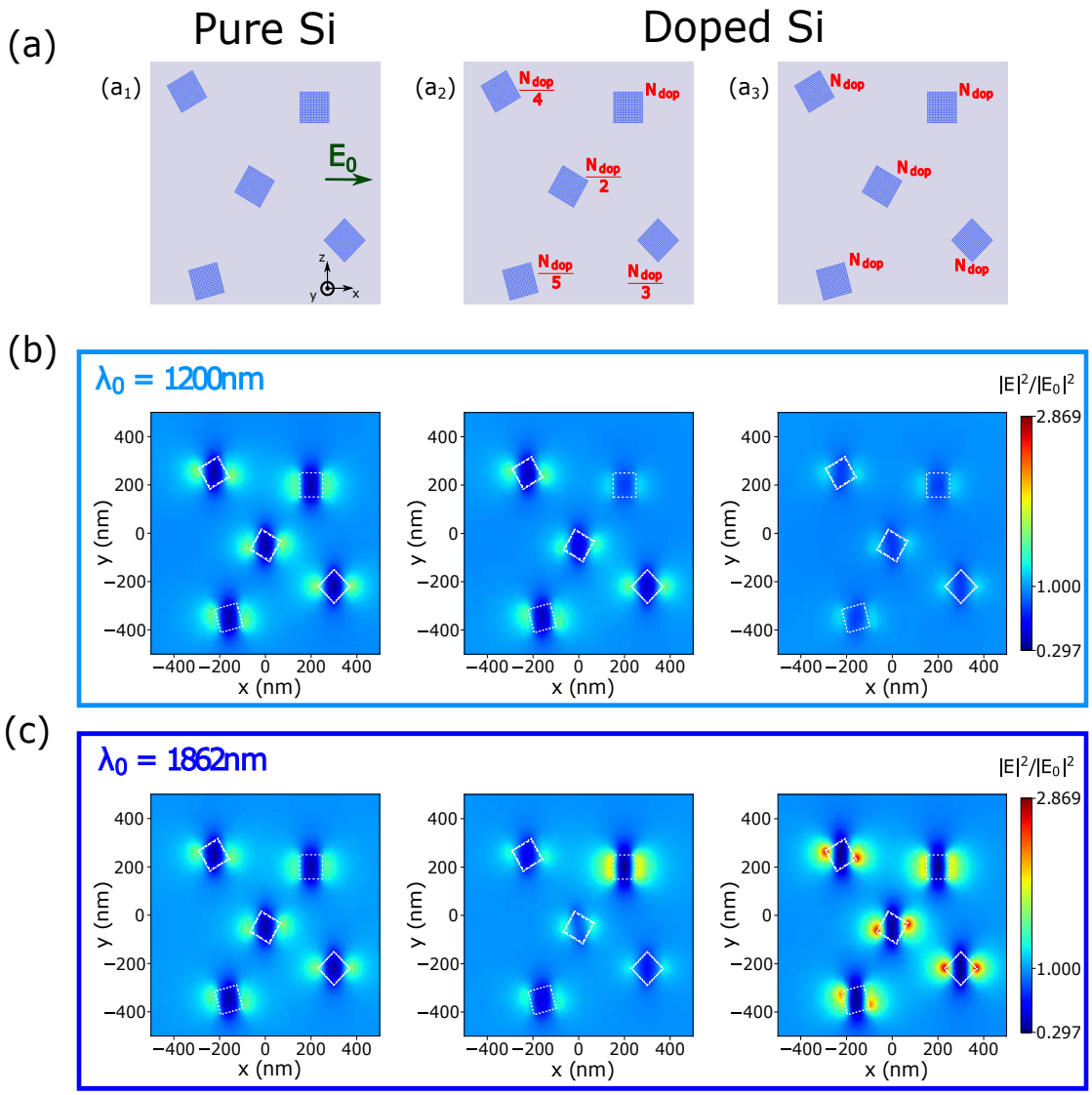

Figure 5: Sequence of optical near–field images describing the evolution of near–field patterns when passing from pure to doped silicon pads. (color scale increasing from blue to red, window size 1000 × 1000 nm^2). All optical and geometrical parameters are identical to those of figure (3). (a) Geometry and dopant concentration considered in the numerical simulations; (b) Near-field map evolution computed at $\lambda_0 = 1200$ nm; (c) Same as (b) but for $\lambda_0 = 1862$ nm.

are potential applications for silicon-based nanophotonics, and study enhanced emission from Erbium ions coupled to hyper-doped Si-NS. In addition, highly localized IR light depression or enhancement can be controlled in the vicinity of the highly doped Si-NS by adjusting the excitation wavelength. This property can be further exploited for either exalting (SERS effect or fluorescence exaltation) or on the contrary hiding (invisibility effect) the optical signal of molecules or nano-objects located in their near field.

These new objects open a new physics field for a mature nano-optics domain. Following up along this simple doping concept, extended networks of interconnected lattices of doped nanoparticles could generate unique and unusual sub-wavelength patterning of the infrared near–field. Several impacts are associated with light confinement around plasmonic structures. The most direct consequence is the improvement of the quality of the near–field infrared imaging and the increased local field enhancement, and finally the light energy storage in tiny volumes of matter [4, 40]. The optical physics related to the control of light confinement might have also important impact on the future solution for the miniaturization of both chemical and biological sensors in the infrared range.

Acknowledgments: This work was supported by the Agence Nationale de la Recherche (project ANR "DONNA" ANR-18-CE09-0034, project NEXT "LANCE" ANR-17-EURE-0009), and the computing facility center (CALMIP) in Toulouse (project P12167).

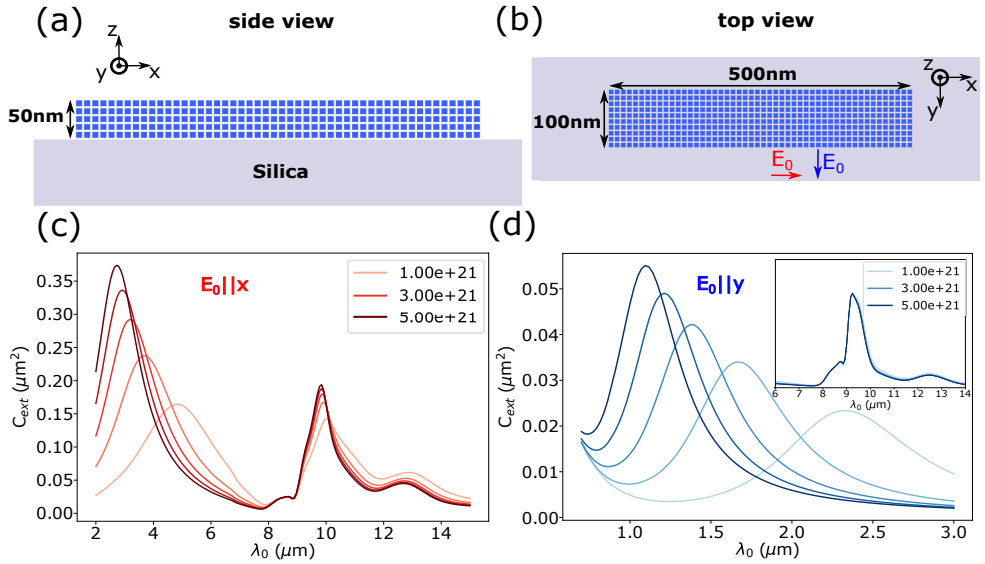

Figure 6: (a) Side view, and (b) top view of the discretized structure of size $500 \times 100 \times 50$ nm^3. The two arrows in (b) represent the polarization of the incident excitation, parallel (red arrow) or perpendicular (blue arrow) to the nanowire axis. (c) Evolution of the extinction cross section due to longitudinal plasmon excitation as function of dopant concentration (from 1×10^{21} to 5×10^{21} cm^{-3}). (d) Same spectrum for transverse plasmon excitation

References

[1] A. G. Brolo, Plasmonics for future biosensors, Nature Photonics 6 (2012) 709–713. doi:10.1038/nphoton.2012.266.
URL https://www.nature.com/articles/nphoton.2012.266

[2] W. L. Barnes, A. Dereux, T. W. Ebbesen, Surface plasmon subwavelength optics, Nature 424 (6950) (2003) 824. doi:10.1038/nature01937.
URL https://www.nature.com/articles/nature01937

[3] Z. W. Seh, S. Liu, M. Low, S.-Y. Zhang, Z. Liu, A. Mlayah, M.-Y. Han, Janus Au-TiO2 Photocatalysts with Strong Localization of Plasmonic Near-Fields for Efficient Visible-Light Hydrogen Generation, Advanced Materials 24 (17) (2012) 2310–2314. doi:10.1002/adma.201104241.
URL https://onlinelibrary.wiley.com/doi/abs/10.1002/adma.201104241

[4] F. Huth, A. Chuvilin, M. Schnell, I. Amenabar, R. Krutokhvostov, S. Lopatin, R. Hillenbrand, Resonant Antenna Probes for Tip-Enhanced Infrared Near-Field Microscopy, Nano Letters 13 (3) (2013) 1065–1072. doi:10.1021/nl304289g.
URL https://doi.org/10.1021/nl304289g

[5] S. Law, L. Yu, A. Rosenberg, D. Wasserman, All-Semiconductor Plasmonic Nanoantennas for Infrared Sensing, Nano Letters 13 (9) (2013) 4569–4574. doi:10.1021/nl402766t.
URL https://doi.org/10.1021/nl402766t

[6] R. Hillenbrand, T. Taubner, F. Keilmann, Phonon-enhanced lightmatter interaction at the nanometre scale, Nature 418 (6894) (2002) 159. doi:10.1038/nature00899.
URL https://www.nature.com/articles/nature00899

[7] J. Aizpurua, T. Taubner, F. J. G. d. Abajo, M. Brehm, R. Hillenbrand, Substrate-enhanced infrared near-field spectroscopy, Optics Express 16 (3) (2008) 1529–1545. doi:10.1364/OE.16.001529.
URL https://www.osapublishing.org/oe/abstract.cfm?uri=oe-16-3-1529

[8] J. M. Luther, P. K. Jain, T. Ewers, A. P. Alivisatos, Localized surface plasmon resonances arising from free carriers in doped quantum dots, Nature Materials 10 (5) (2011) 361–366. doi:10.1038/nmat3004.
URL https://www.nature.com/articles/nmat3004

[9] N. J. Kramer, K. S. Schramke, U. R. Kortshagen, Plasmonic Properties of Silicon Nanocrystals Doped with Boron and Phosphorus, Nano Letters 15 (8) (2015) 5597–5603. doi:10.1021/acs.nanolett.5b02287.
URL https://doi.org/10.1021/acs.nanolett.5b02287

[10] J. A. Faucheaux, A. L. D. Stanton, P. K. Jain, Plasmon Resonances of Semiconductor Nanocrystals: Physical Principles and New Opportunities, The Journal of Physical Chemistry Letters 5 (6) (2014) 976–985. doi:10.1021/jz500037k.
URL https://doi.org/10.1021/jz500037k

[11] I. Kriegel, F. Scotognella, L. Manna, Plasmonic doped semiconductor nanocrystals: Properties, fabrication, applications and perspectives, Physics Reports 674 (2017) 1–52. doi:10.1016/j.physrep.2017.01.003.
URL http://www.sciencedirect.com/science/article/pii/S0370157317300364

[12] X. Pi, C. Delerue, Tight-Binding Calculations of the Optical Response of Optimally P-Doped Si Nanocrystals: A Model for Localized Surface Plasmon Resonance, Physical Review Letters 111 (17) (2013) 177402. doi:10.1103/PhysRevLett.111.177402.
URL https://link.aps.org/doi/10.1103/PhysRevLett.111.177402

[13] F. Della Sala, M. Pezzolla, S. DAgostino, E. Fabiano, Ab Initio Plasmonics of Externally Doped Silicon Nanocrystals, ACS Photonicsdoi:10.1021/acsphotonics.9b00126.
URL https://doi.org/10.1021/acsphotonics.9b00126

[14] R. Guerra, S. Ossicini, Preferential Positioning of Dopants and Co-Dopants in Embedded and Freestanding Si Nanocrystals, Journal of the American Chemical Society 136 (11) (2014) 4404–4409. doi:10.1021/ja5002357.
URL https://doi.org/10.1021/ja5002357

[15] D. J. Rowe, J. S. Jeong, K. A. Mkhoyan, U. R. Kortshagen, Phosphorus-Doped Silicon Nanocrystals Exhibiting Mid-Infrared Localized Surface Plasmon Resonance, Nano Letters 13 (3) (2013) 1317–1322. doi:10.1021/nl4001184.
URL https://doi.org/10.1021/nl4001184

[16] L. M. Wheeler, N. R. Neale, T. Chen, U. R. Kortshagen, Hypervalent surface interactions for colloidal stability and doping of silicon nanocrystals, Nature Communications 4 (2013) 2197. doi:10.1038/ncomms3197.
URL https://www.nature.com/articles/ncomms3197

[17] P. R. Wiecha, C. Majorel, C. Girard, A. Arbouet, B. Masenelli, O. Boisron, A. Lecestre, G. Larrieu, V. Paillard, A. Cuche, En-

hancement of electric and magnetic dipole transition of rare-earth-doped thin films tailored by high-index dielectric nanostructures, Applied Optics 58 (7) (2019) 1682–1690. doi:10.1364/AO.58.001682.
URL https://www.osapublishing.org/ao/abstract.cfm?uri=ao-58-7-1682

[18] K. Huet, F. Mazzamuto, T. Tabata, I. Toqu-Tresonne, Y. Mori, Doping of semiconductor devices by Laser Thermal Annealing, Materials Science in Semiconductor Processing 62 (2017) 92–102. doi:10.1016/j.mssp.2016.11.008.
URL http://www.sciencedirect.com/science/article/pii/S1369800116305017

[19] P. Acosta Alba, S. Kerdiles, B. Mathieu, R. Kachtouli, F. Mazzamuto, I. Toque-Tresonne, K. Huet, P. Besson, M. Veillerot, F. Aussenac, C. Fenouillet-Beranger, Nanosecond Laser Annealing for Phosphorous Activation in Ultra-Thin Implanted Silicon-On-Insulator Substrates, in: 2016 21st International Conference on Ion Implantation Technology (IIT), IEEE, Tainan, Taiwan, 2016, pp. 1–4. doi:10.1109/IIT.2016.7882896.
URL http://ieeexplore.ieee.org/document/7882896/

[20] M. Wang, A. Debernardi, Y. Berencn, R. Heller, C. Xu, Y. Yuan, Y. Xie, R. Bttger, L. Rebohle, W. Skorupa, M. Helm, S. Prucnal, S. Zhou, Breaking the Doping Limit in Silicon by Deep Impurities, Physical Review Applied 11 (5) (2019) 054039. doi:10.1103/PhysRevApplied.11.054039.
URL https://link.aps.org/doi/10.1103/PhysRevApplied.11.054039

[21] P. R. Wiecha, pyGDMA python toolkit for full-field electrodynamical simulations and evolutionary optimization of nanostructures, Computer Physics Communications 233 (2018) 167–192. doi:10.1016/j.cpc.2018.06.017.
URL http://www.sciencedirect.com/science/article/pii/S001046551830225X

[22] C. Girard, Near fields in nanostructures, Reports on Progress in Physics 68 (8) (2005) 1883. doi:10.1088/0034-4885/68/8/R05.
URL http://stacks.iop.org/0034-4885/68/i=8/a=R05

[23] S. Zhou, X. Pi, Z. Ni, Y. Ding, Y. Jiang, C. Jin, C. Delerue, D. Yang, T. Nozaki, Comparative Study on the Localized Surface Plasmon Resonance of Boron- and Phosphorus-Doped Silicon Nanocrystals, ACS Nano 9 (1) (2015) 378–386. doi:10.1021/nn505416r.
URL https://doi.org/10.1021/nn505416r

[24] M. Cada, D. Blazek, J. Pistora, K. Postava, P. Siroky, Theoretical and experimental study of plasmonic effects in heavily doped gallium arsenide and indium phosphide, Optical Materials Express 5 (2) (2015) 340–352. doi:10.1364/OME.5.000340.
URL https://www.osapublishing.org/ome/abstract.cfm?uri=ome-5-2-340

[25] M. Soltani, R. Soref, Free-carrier electrorefraction and electroabsorption in wurtzite GaN, Optics Express 23 (19) (2015) 24984–24990. doi:10.1364/OE.23.024984.
URL https://www.osapublishing.org/oe/abstract.cfm?uri=oe-23-19-24984

[26] C. Girard, E. Dujardin, G. Baffou, R. Quidant, Shaping and manipulation of light fields with bottom-up plasmonic structures, New Journal of Physics 10 (10) (2008) 105016. doi:10.1088/1367-2630/10/10/105016.
URL https://doi.org/10.1088%2F1367-2630%2F10%2F10%2F105016

[27] B. T. Draine, The discrete-dipole approximation and its application to interstellar graphite grains, The Astrophysical Journal 333 (1988) 848–872. doi:10.1086/166795.
URL http://adsabs.harvard.edu/abs/1988ApJ...333..848D

[28] R. Marty, G. Baffou, A. Arbouet, C. Girard, R. Quidant, Charge distribution induced inside complex plasmonic nanoparticles, Optics Express 18 (3) (2010) 3035–3044. doi:10.1364/OE.18.003035.
URL https://www.osapublishing.org/oe/abstract.cfm?uri=oe-18-3-3035

[29] M. K. Gunde, Vibrational modes in amorphous silicon dioxide, Physica B: Condensed Matter 292 (3) (2000) 286–295. doi:10.1016/S0921-4526(00)00475-0.
URL http://www.sciencedirect.com/science/article/pii/S0921452600004750

[30] R. Kitamura, L. Pilon, M. Jonasz, Optical constants of silica glass from extreme ultraviolet to far infrared at near room temperature 46 (33) (2007) 8118–8133.
URL https://escholarship.org/uc/item/0st1d3tg

[31] R. Marty, A. Mlayah, A. Arbouet, C. Girard, S. Tripathy, Plasphonics : local hybridization of plasmons and phonons, Optics Express 21 (4) (2013) 4551–4559. doi:10.1364/OE.21.004551.
URL https://www.osapublishing.org/oe/abstract.cfm?uri=oe-21-4-4551

[32] R. Hillenbrand, T. Taubner, F. Keilmann, Phonon-enhanced lightmatter interaction at the nanometre scale, Nature 418 (6894) (2002) 159–162. doi:10.1038/nature00899.
URL http://www.nature.com/articles/nature00899

[33] M. S. Anderson, Surface enhanced infrared absorption by coupling phonon and plasma resonance, Applied Physics Letters 87 (14) (2005) 144102. doi:10.1063/1.2077838.
URL https://aip.scitation.org/doi/10.1063/1.2077838

[34] L. Novotny, Effective Wavelength Scaling for Optical Antennas, Physical Review Letters 98 (26) (2007) 266802. doi:10.1103/PhysRevLett.98.266802.
URL https://link.aps.org/doi/10.1103/PhysRevLett.98.266802

[35] A. Dibos, M. Raha, C. Phenicie, J. Thompson, Atomic Source of Single Photons in the Telecom Band, Physical Review Letters 120 (24). doi:10.1103/PhysRevLett.120.243601.
URL https://link.aps.org/doi/10.1103/PhysRevLett.120.243601

[36] D. Barchiesi, C. Girard, O. J. F. Martin, D. Van Labeke, D. Courjon, Computing the optical near-field distributions around complex subwavelength surface structures: A comparative study of different methods, Physical Review E 54 (4) (1996) 4285–4292. doi:10.1103/PhysRevE.54.4285.
URL https://link.aps.org/doi/10.1103/PhysRevE.54.4285

[37] J.-C. Weeber, E. Bourillot, A. Dereux, J.-P. Goudonnet, Y. Chen, C. Girard, Observation of Light Confinement Effects with a Near-Field Optical Microscope, Physical Review Letters 77 (27) (1996) 5332–5335. doi:10.1103/PhysRevLett.77.5332.
URL https://link.aps.org/doi/10.1103/PhysRevLett.77.5332

[38] S. Link, M. A. El-Sayed, Shape and size dependence of radiative, non-radiative and photothermal properties of gold nanocrystals, International Reviews in Physical Chemistry 19 (3) (2000) 409–453. doi:10.1080/01442350050034180.
URL https://doi.org/10.1080/01442350050034180

[39] S. Link, M. A. El-Sayed, Spectral Properties and Relaxation Dynamics of Surface Plasmon Electronic Oscillations in Gold and Silver Nanodots and Nanorods, The Journal of Physical Chemistry B 103 (40) (1999) 8410–8426. doi:10.1021/jp9917648.
URL https://doi.org/10.1021/jp9917648

[40] F. Huth, A. Govyadinov, S. Amarie, W. Nuansing, F. Keilmann, R. Hillenbrand, Nano-FTIR Absorption Spectroscopy of Molecular Fingerprints at 20 nm Spatial Resolution, Nano Letters 12 (8) (2012) 3973–3978. doi:10.1021/nl301159v.
URL https://doi.org/10.1021/nl301159v